



Slag characterisation of 308L-type stainless steel rutile flux-cored wires

Sylvia Holly¹ · Peter Mayer² · Christian Bernhard² · Gerhard Posch³

Received: 11 October 2017 / Accepted: 12 November 2018 / Published online: 29 November 2018
© International Institute of Welding 2018

Abstract

The behaviour of the weld characteristic of flux-cored wires is strongly influenced by the flux. The weld metal and weldability are determined by the flux composition and to a much smaller level by shielding gas used as well. The wide variety of components combined with the complexity of the welding process result in intricate mechanisms occurring in the slag. The slags of the different rutile flux-cored wires, designed for either position or standard downhand welding, were analysed in order to gain knowledge about the complex slag mechanisms and to carry out a metallurgical characterisation. Chemical analysis, differential thermal analysis and microstructural investigations of the slags were conducted to identify and characterise the formed phases. In addition, the viscosities of the slags were measured and correlated with the DTA results.

Keywords Slag characterisation · Flux-cored wires · DTA · HT-LSCM · Viscosity

1 Introduction

Shielded metal arc welding (SMAW) is a very famous welding process with high capabilities in respect to weld metallurgy, welding behaviour and welding technique based on their special slags but with almost no economic option for automation. That is why industry is anxious to introduce comparable, but highly economic processes and flux-cored arc welding (FCAW) is thereby a process of choice.

The huge range of available stick electrodes can be conveniently classified into three main groups based on their coating composition and in further consequence on their slag system as rutile, basic and cellulosic types. Each of them gives the electrode a distinctive set of welding and metallurgical characteristics. Basic coatings provide best metallurgical properties but have a restricted welding behaviour especially in vertical and overhead positions. Their main constituents are

calcium fluoride, calcium carbonate and other alkaline carbonates. These substances make the resulting slag metallurgical active but more viscous and fast-freezing. Basic-coated electrodes also have a coarse droplet material transfer. In contrast, rutile coatings provide a fine droplet transfer and best welding characteristics in all welding positions. They contain a large amount of titanium dioxide in addition to calcium carbonate, silica and magnetite. Rutile electrodes produce a dense slag covering which yields to a smooth, evenly rippled weld surface and can easily be removed. Nevertheless, the mechanical properties of the weld metals are moderate in comparison to basic electrodes due to their limited metallurgical slag activity, but the welding behaviour is excellent.

In any case, the electrodes have to generate a shielding gas during welding to secure a stable electric arc. This will be achieved by dissociation of carbonates which are added to the coating which limits the freedom in slag design.

FCAW combines the benefits of SMAW and Gas Metal Arc Welding: high metallurgical activity in combination with high deposition rates, out of position weldability and high grades of automation. This depends on the flux design of the particular wire. The therefore used flux-cored wires consist of metallic tubes in typical GMAW wire diameters, which are filled with special fluxes. The development of flux-cored wires targets to combine the advantages of solid wires, for instance their automation possibilities, with those of stick electrodes, particularly their slag effects. Additionally, the process-related existence of an external shielding gas allows more freedom in flux design. The fluxes are composed of a

Recommended for publication by Commission IX - Behaviour of Metals Subjected to Welding

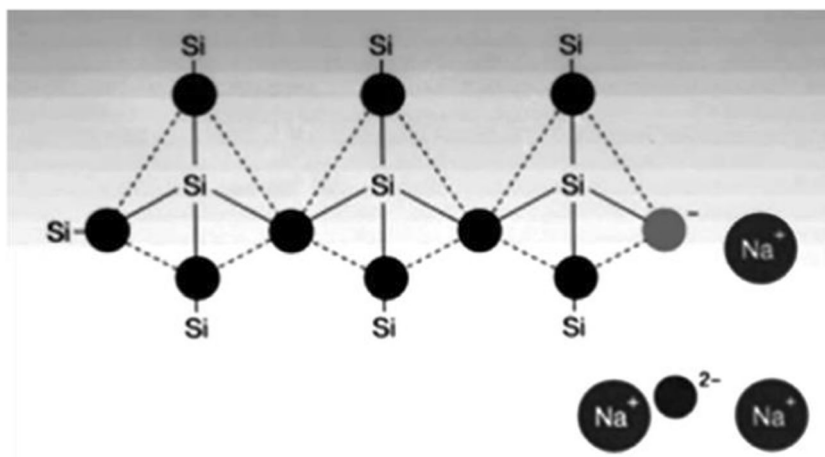
✉ Sylvia Holly
sylvia.holly@voestalpine.com

¹ voestalpine Böhler Welding Austria GmbH, Böhler Welding Str. 1, A-8605 Kapfenberg, Austria

² Department of Ferrous Metallurgy, Montanuniversitaet Leoben, A-8700 Leoben, Austria

³ Fronius International GmbH, Froniusplatz 1, A-4600 Wels, Austria

Fig. 1 Schematic illustration of network forming with bridging oxygens and forming of non-bridging-oxygen [17, 18]



dedicated mixture of various metallic and non-metallic powders. The main functions of the metallic ingredients are to control the weld metal chemistry and to optimise the mechanical properties of the weld metal. The non-metallic ingredients are responsible for establishing an adequate slag and to secure a stable arc in combination with a smooth droplet transfer. They can also provide a secondary gas shielding and support the purification of the weld metal. The non-metallic ingredients also help to reduce spattering and control the melting characteristics of the electrode. These slag-forming components are added as powder to the flux, whereby basic and rutil concepts can be established. Owing to their better welding characteristics and positional weldability, rutil concepts have found widespread use.

In FCAW, mainly two different kinds of rutil slags are used. Slags for horizontal welding with viscosities increase continuously within a certain temperature range. There are no special temperatures, so-called break points, at which the solidification behaviour changes significantly. Furthermore, they possess a higher basic viscosity, which is important for seam coverage [1]. On the other hand, slags for vertical welding have narrow solidification temperature ranges and supporting effects in respect to the deposited liquid metal. Their solidification behaviour is characterised by break points at certain temperatures and, compared to slags for horizontal welding, they possess a lower viscosity at high temperatures before they reach the break point temperature, which is referred to as basic viscosity. As they solidify earlier than the liquid weld metal, they act as a formwork for the liquid weld which is the basis for a good out-of-position weldability.

Table 1 All-weld metal chemical composition of investigated flux-cored wires

	C	Si	Mn	Cr	Ni	Mo	Nb
T 19 9 L R M21 3/E308LT0-4	0.03	0.7	1.5	19.8	10.5	–	–
T 19 9 L P M21 1/E308LT1-4	0.03	0.7	1.5	19.8	10.5	–	–

Within the scope of this paper, two rutil austenitic stainless steel flux-cored wire concepts, one for horizontal and one for out-of-position welding, are compared and characterised.

2 Slag theory

According to literature [2–6], liquid slags show an ionic behaviour and consist of (I) cations such as Ca^{2+} and Fe^{2+} , (II) anions such as O^{2-} , F^{2-} and S^{2-} and finally (III) anion complexes such as SiO_4^{4-} and AlO_3^{2-} [7]. The anion complexes such as SiO_4^{4-} usually form networks by bridging oxygens. Cations like Ca^{2+} or Mg^{2+} tend to break these networks and form either non-bridging oxygens or free oxygen anions O^{2-} . The so-called depolymerisation of a slag depends on the ratio of non-bridging oxygen vs. anion complexes and so do most physical properties, such as viscosity or thermal conductivity [8]. Whereas the role of SiO_2 is clearly defined to be a network former, Fe^{2+} tends to operate as network breaker and Fe^{3+} as a network former and breaker [9, 10]. In TiO_2 -containing slags, Ti^{4+} acts usually as a network former up to moderate TiO_2 content whereas it can be both a network former and a network breaker at elevated TiO_2 content. The role of some slag components for the thermophysical properties of a slag is therefore still unclear, mainly for less extensively investigated slag systems such as welding slags.

In a very generalised form, the basicity of a slag is the ratio between network breakers and network formers. The characterisation of slags using basicity indices is well established in

Table 2 Welding parameters used for production of slag samples

Wire	Voltage [V]	Current min/max [A]	Welding speed [m/min]	Wire feed speed [m/min]	Heat input [kJ/m]
E308LT0-4	28.3	214/250	0.4	12.0	787.87
E308LT1-4	28.3	216/246	0.4	12.0	784.48

Table 3 Comparison of the slag chemistries, extrapolated with the Omnian method [22]

Component	E308LT0-4	E308LT1-4
SiO ₂ [m%]	10.9	3.6
ZrO ₂ [m%]	21.5	8.3
MnO [m%]	14.6	8.5
Cr ₂ O ₃ [m%]	16.4	13.9
TiO ₂ [m%]	30.1	58.7
F [m%]	0.75	0.32

the welding industry owing to the correlation between oxygen potential, viscosity and basicity [11, 12].

The roles of welding slags are to protect the liquid metal and its solidifying surface from environmental effects and to remove undesirable elements. The slag viscosity should be high enough to protect the surface and low enough to ensure gas permeability. Low viscosity slags are required for the removal of undesired elements owing to their higher diffusion coefficient, whereas high viscosity isolates the metal resulting in deeper penetration [13]. That is why the development of welding slag systems is challenging. It is evident that within the welding slag formation process TiO₂ is an important component and it is the main constituent for rutile slags. Knowledge about the effects of TiO₂ in multi-component systems is derived from the SiO₂-TiO₂ system, but the findings in the literature are contradictory [4]. For example TiO₂ can be classified as a network former [4] as well as network breaker [14]. It decreases viscosity when present in the content range from 0 to 5 m% owing to depolymerisation [15, 16].

Figure 1 shows a schematic depiction of the forming networks.

There is a correlation between the structure and the physical properties of slags, which can be described using different parameters, such as basicity indices and degree of polymerisation, whereby the basicity indices are based on the ratio between acid and basic components [9, 10, 19–21].

3 Experimental

3.1 Materials

Slags of two different kinds of austenitic 308L-type flux-cored wires, one designed for flat T0 position and one for T1 position welding, were produced by melting down the flux-cored wire. Afterwards, pieces of the slag were collected and investigated. As shielding gas M21 (Ar+18%CO₂) was used. Austenitic steel sheets with a thickness of 10 mm were used as the base material. The chemical composition of the all weld metal is listed in Table 1, the welding parameters are listed in Table 2 and the correspondent slag chemistries in Table 3.

The slags were prepared by manual welding in flat and horizontal position.

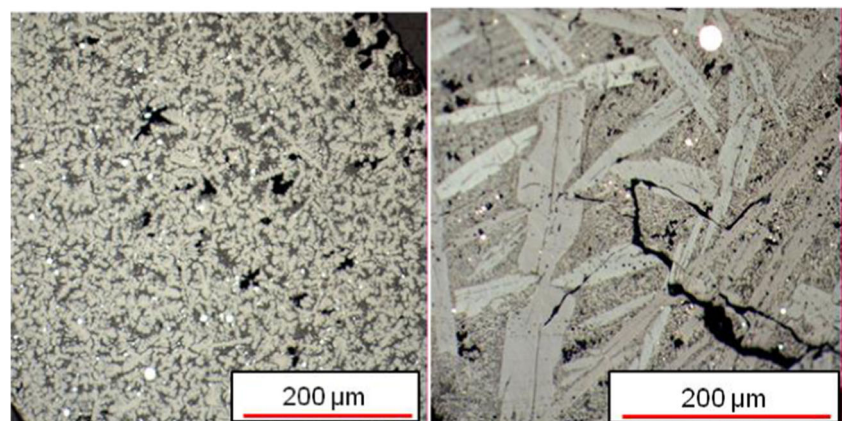
The chemical analysis was done using X-ray fluorescence spectrometry. The samples were milled with ZrO₂ grinding balls that were homogenised and processed to pressed pellets. The contents were evaluated with the Omnian software package.

3.2 Slag composition

The chemical composition of the slags was measured at low vacuum using EDX. As this method only provides the total amount of the elements without any differentiation between metallic and non-metallic phases and also the oxygen content is due to the low vacuum slightly overestimated, the software Omnian was used to express metals and oxides under consideration of the oxidation state. The chemical composition of the main components of the two slags is listed in Table 3.

The chemical analyses of the slags are significantly different. A comparison of the concentrations shows an obviously higher TiO₂ content in the slag of the positional welding wire than in the slag of the flat position welding wire. This is because TiO₂ is of vital importance regarding vertical position welding. However, the slag of E308LT0-4 exhibits higher

Fig. 2 Microstructure of E308LT0-4 slag (left) and E308LT1-4 slag (right)



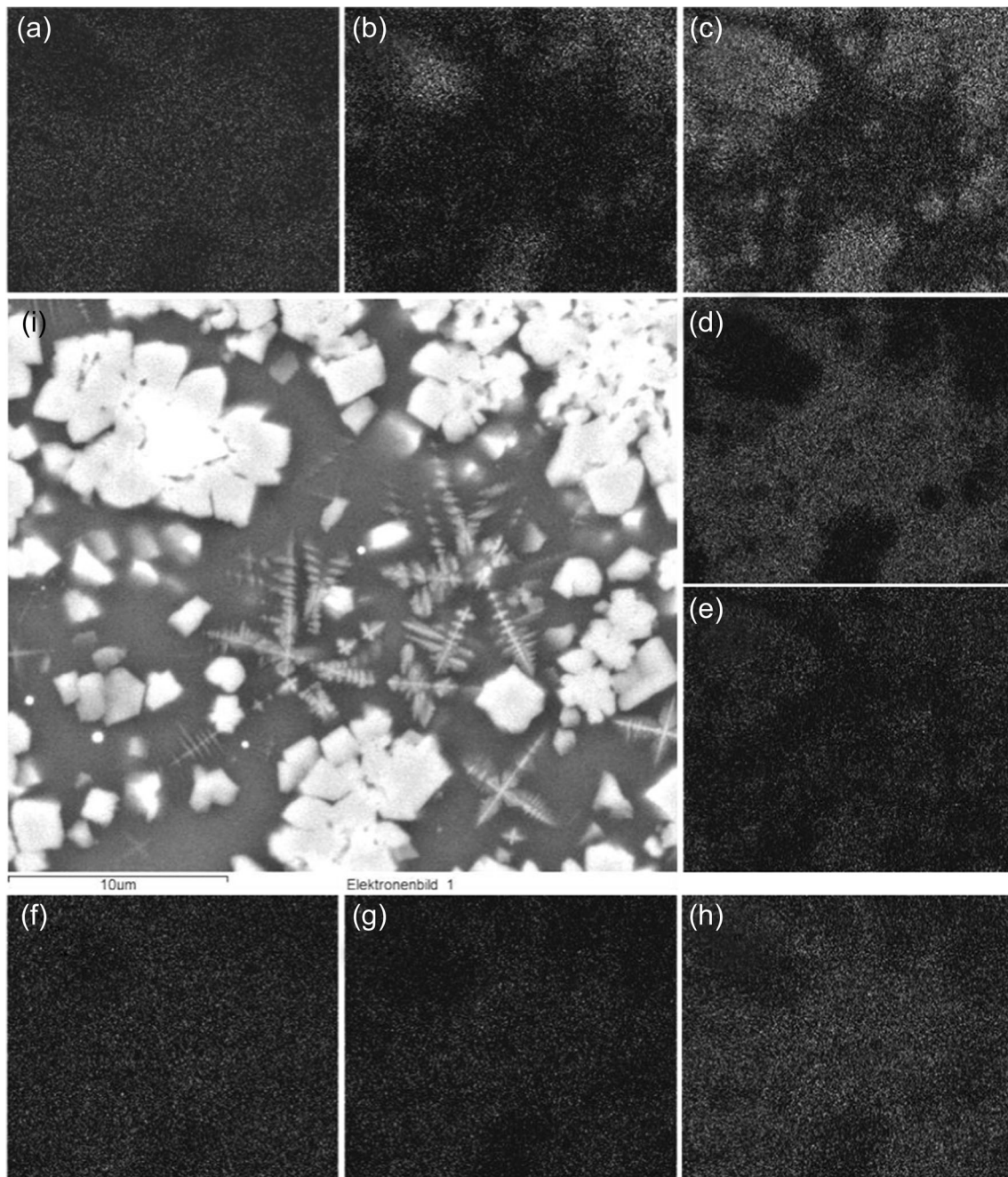


Fig. 3 Mapping of the elements **a** Na, **b** Zr, **c** Ti, **d** Si, **e** Cr, **f** Mn, **g** Al and **h** O across the area depicted in **i**

contents of ZrO_2 , MnO and SiO_2 , and the amount of fluorine is more than twice as high.

3.3 Microstructure

The slags resulting from the welding process were examined by light optical microscopy (OM) and scanning electron microscopy (SEM). Araldite DBF was used as embedding resin for the microsection analysis, and the samples were prepared using standard metallographic

techniques. The samples were investigated using the Nikon MM40 light optical microscope and CLEMEX Vision 3.5 software. The energy dispersive X-ray spectroscopy (EDX) investigations were performed using QUANTA 200 Mk2 SEM with an Oxford Energy 200 detector and Inca software. SEM was used for identification of phases and to measure the chemistry via EDX. Mapping of the slag areas was also conducted.

The OM investigations clearly clarify the differences between the slag systems of the wires, as shown in

Fig. 4 SEM images of slag E308LT0-4 with different magnifications: **a** entire cross section; **b** positions of spectra

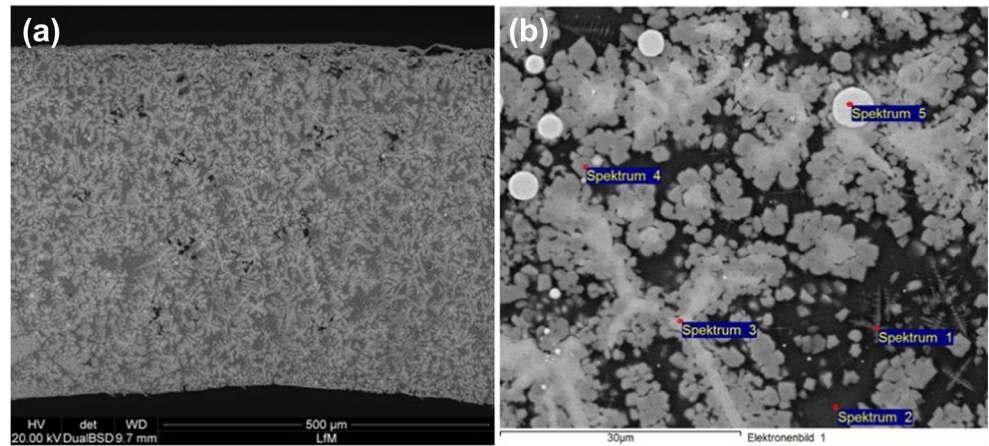
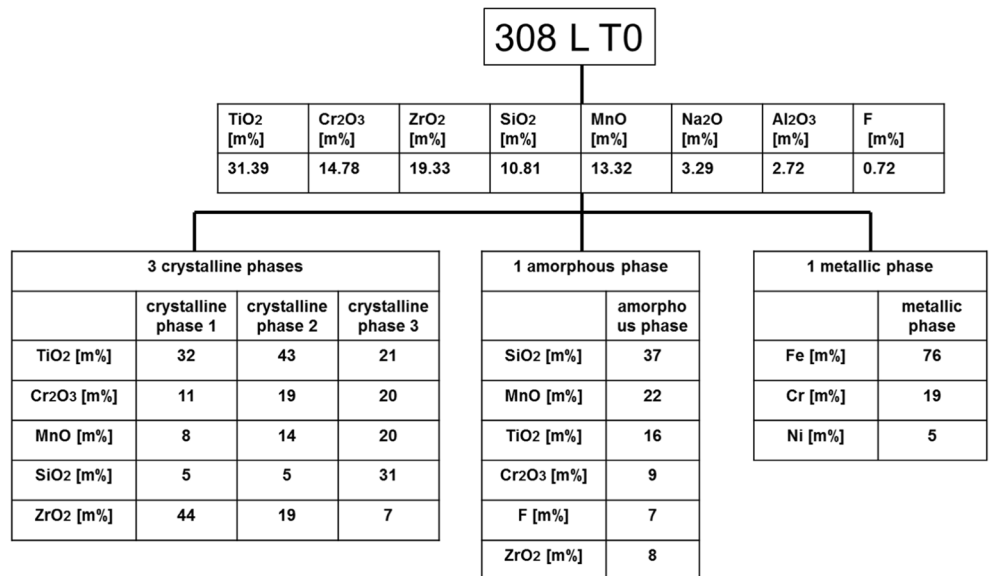


Table 4 EDX analysis results of measurement points in Fig. 4

Spectra	Na ₂ O [m%]	Al ₂ O ₃ [m%]	SiO ₂ [m%]	K ₂ O [m%]	CaO [m%]	TiO ₂ [m%]	Cr ₂ O ₃ [m%]	MnO [m%]	Fe [m%]	ZrO ₂ [m%]	F [m%]	Ni [m%]	Cr [m%]
1	4.31	5.43	27.97	0.86	0.00	18.76	18.23	18.05	0.00	6.38	0.00	0.00	0.00
2	5.73	5.88	32.47	0.79	0.87	13.87	8.09	19.32	0.00	6.65	6.34	0.00	0.00
3	1.41	0.00	4.58	0.00	0.00	32.06	11.12	8.10	0.00	42.73	0.00	0.00	0.00
4	0.00	2.04	5.40	0.00	0.00	42.05	18.83	13.30	0.00	18.37	0.00	0.00	0.00
5	0.00	0.00	5.46	0.00	0.00	10.96	0.00	4.37	55.27	6.54	0.00	3.62	13.77

Fig. 5 Classification of slag phases for E308LT0-4.



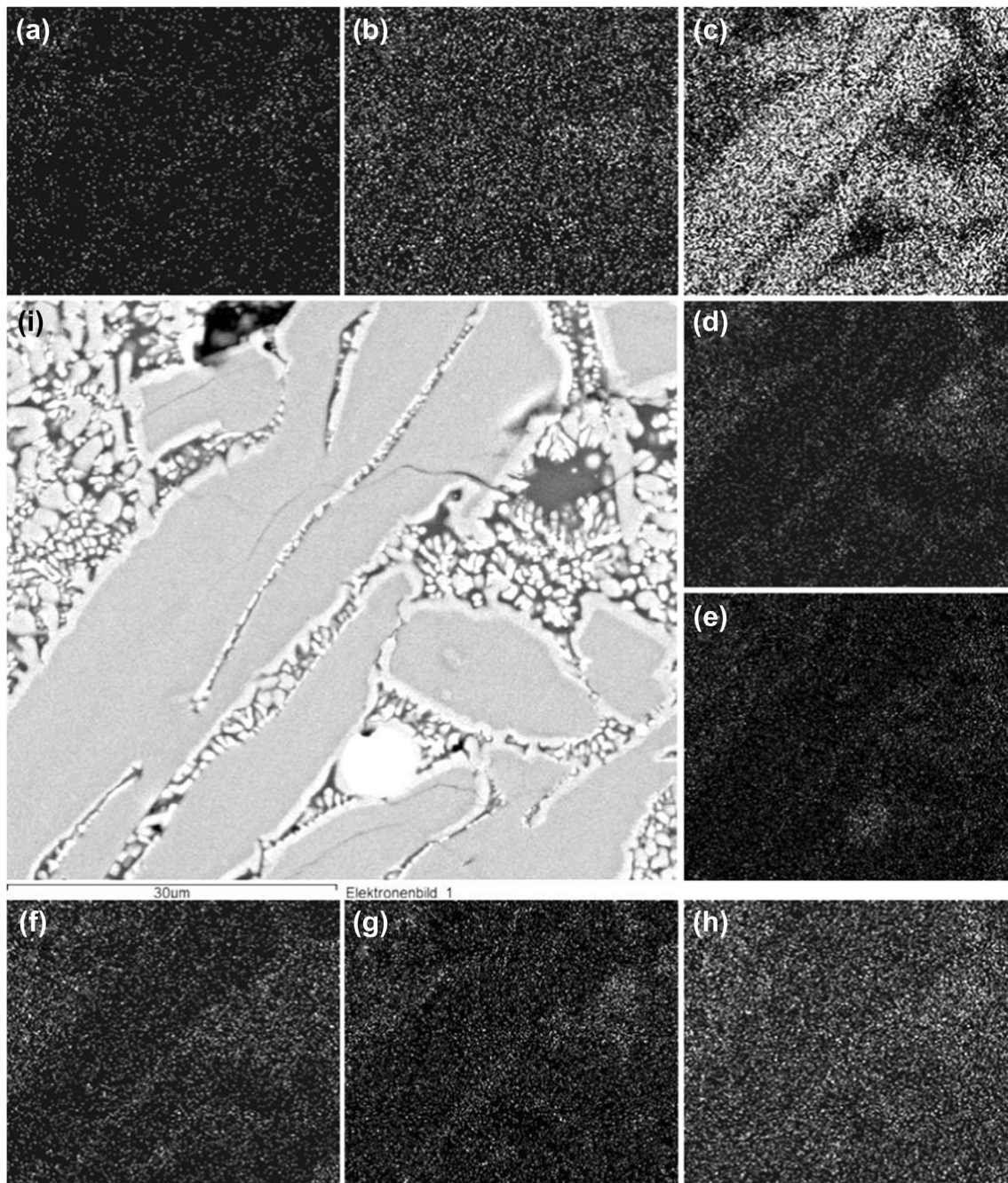


Fig. 6 Mapping of the elements **a** Na, **b** Zr, **c** Ti, **d** Si, **e** Cr, **f** Mn, **g** Al and **h** O across the area depicted in **i** for E308LT1-4

Fig. 2. The E308LT0-4 slag exhibited a fine crystalline structure, embedded in a glassy matrix. The microstructure of the E308LT1-4 slag was coarse grained, including coarsened columnar crystals in a glassy matrix. This may explain the suitability of these slags for vertical positions owing to the higher supporting effect by the precipitation of these crystals.

SEM was used to characterise the distribution of the elements, and EDX was performed to identify the chemical composition.

3.4 E308LT0-4 type slag

The distribution of the elements via mapping is illustrated in Fig. 3. Differences in the composition based on crystalline and amorphous phase contents were discernible. Ti, Zr and Cr were mainly detected in the crystalline-solidified area, whereas Si, Mn, and Al were determined in the amorphous area.

Subsequently, the phases were characterised based on their chemical composition via EDX measurements. The

Fig. 7 SEM images of slag E308LT1-4 with different magnifications **a** entire cross section; **b** positions of spectra

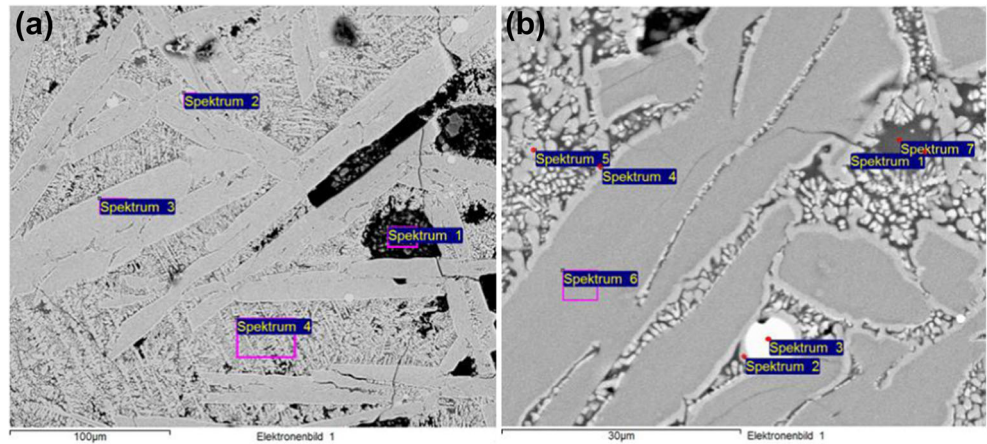


Table 5 EDX analysis results of measurement points in Fig. 7

Spectrum	Na ₂ O [m%]	Al ₂ O ₃ [m%]	SiO ₂ [m%]	K ₂ O [m%]	CaO [m%]	TiO ₂ [m%]	Cr ₂ O ₃ [m%]	MnO [m%]	Fe [m%]	ZrO ₂ [m%]	F [m%]	Ni [m%]	Cr [m%]
Fig. 7a	1	0.00	4.02	2.97	0.00	50.87	33.45	5.64	3.04	0.00	0.00	0.00	0.00
	2	1.42	2.95	1.73	0.00	0.00	20.99	0.00	2.84	48.30	2.77	0.00	19.01
	3	0.00	5.35	1.27	0.00	0.00	78.17	6.78	2.64	0.00	5.79	0.00	0.00
	4	2.62	9.48	7.72	1.40	0.64	45.13	15.62	8.79	0.00	8.59	0.00	0.00
Fig. 7b	1	2.75	11.32	8.36	1.30	0.00	42.64	12.67	8.94	0.00	12.01	0.00	0.00
	2	0.00	5.08	2.35	0.00	0.00	45.86	22.68	6.95	12.61	4.46	0.00	0.00
	3	0.00	3.83	0.00	0.00	0.00	22.24	0.00	2.49	47.34	3.43	0.00	1.46
	4	1.35	6.10	3.16	0.00	0.00	59.39	16.73	8.49	0.00	4.77	0.00	0.00
	5	0.00	6.32	3.05	0.59	0.00	57.23	19.18	9.10	0.00	4.53	0.00	0.00
	6	0.00	4.80	1.60	0.00	0.00	79.00	6.68	3.10	0.00	4.81	0.00	0.00
	7	6.68	18.73	22.56	3.76	0.85	23.94	5.18	7.18	0.76	3.76	6.59	0.00

Fig. 8 Classification of slag phases for E308LT1-4.

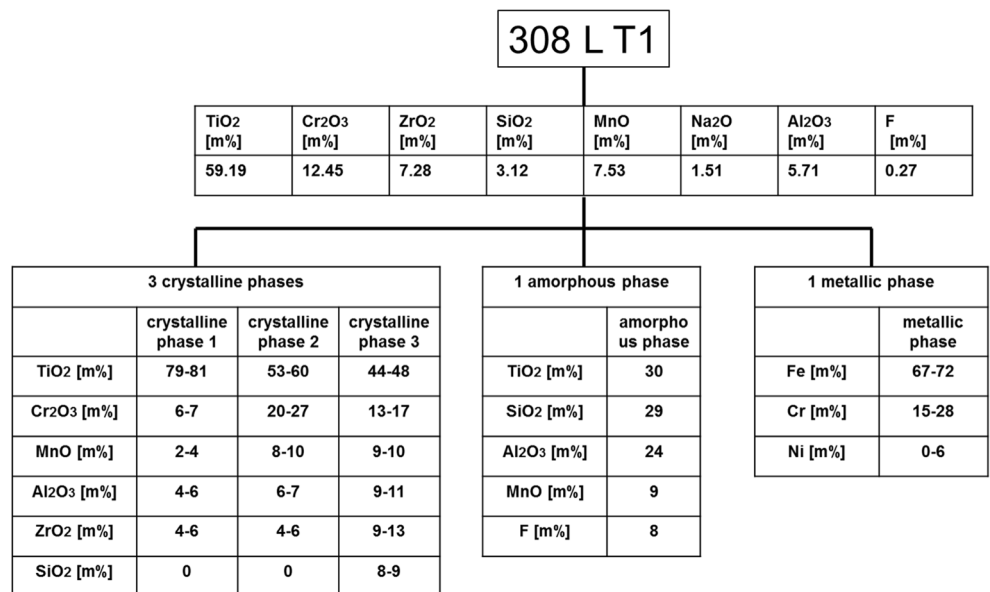


Fig. 9 **a** SEM image of E308LT0-4 slag; **b** depiction of single phases: blue-amorphous phase, yellow-metallic phase, violet-crystalline phase 1, green-crystalline phase 2, and red-crystalline phase 3

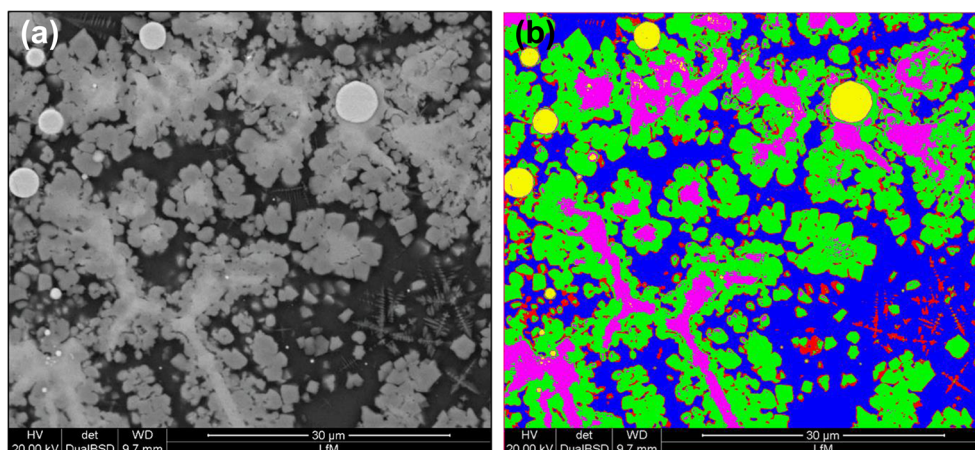
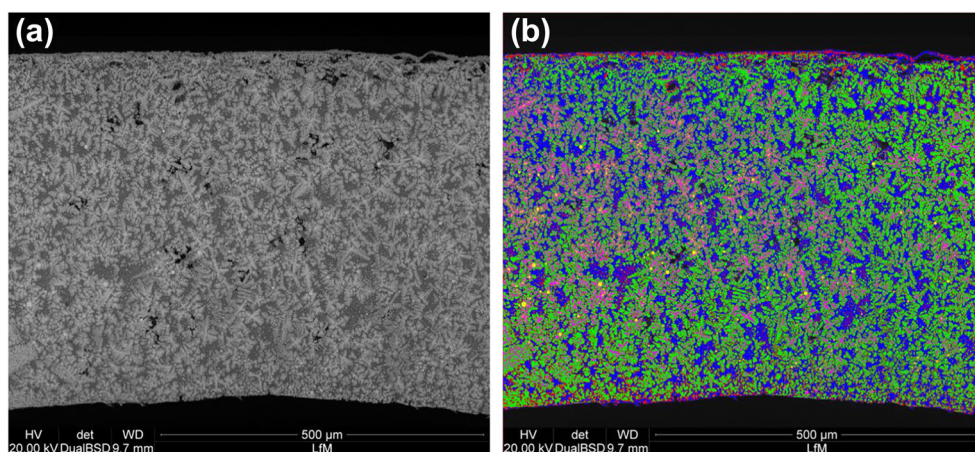


Fig. 10 **a** SEM image of E308LT0-4 slag; **b** depiction of single phases: blue-amorphous phase, yellow-metallic phase, violet-crystalline phase 1, green-crystalline phase 2, and red-crystalline phase 3



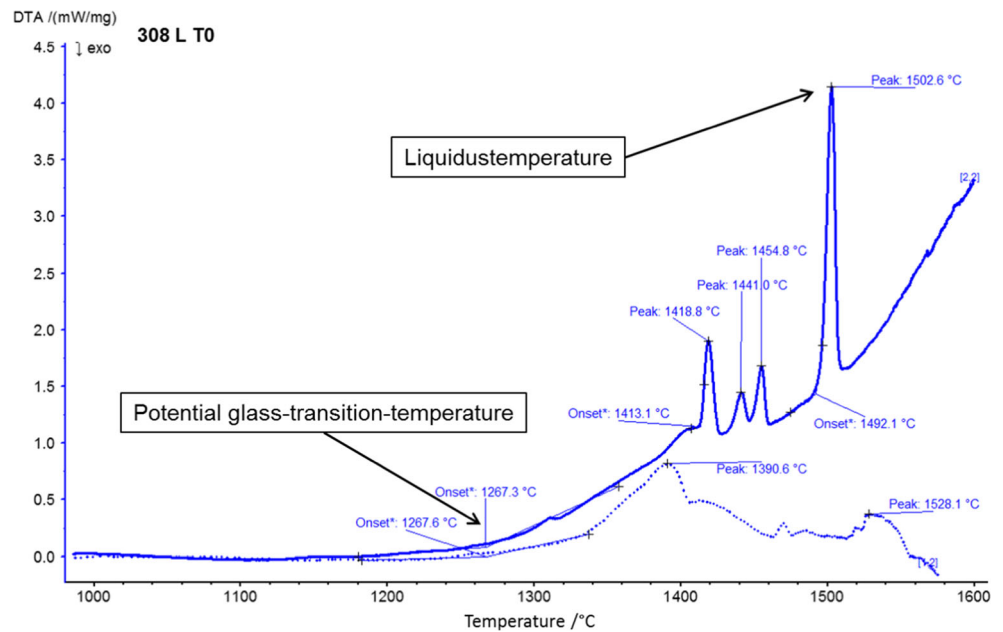
images and measurement positions are shown in Fig. 4. Table 4 lists the corresponding chemical analyses of the certain positions, which were extrapolated to the respective oxides. It can be assumed that fluoride exists as a compound, but no indication about the nature of this compound is given, whereas the fluoride contents are presented in the list.

Table 6 Phase fractions of E308LT0-4 slag.

Phase	Phase fraction in Fig. 9 [%]	Area fraction Error! Reference source not found.0 [%]
Crystalline phase 1	12	3
Crystalline phase 2	45	54
Crystalline phase 3	10	5
Amorphous phase	32	38
Metallic phase	2	1
Amorphous/crystalline	48	63

By comparing the results of the chemical analyses with those of the SEM investigation, it is clear that the slag consists of three crystalline phases (spectra 1, 3 and 4), one amorphous phase (spectrum 2) and one metallic phase (spectrum 5). The images show that no interlocking occurred within the crystalline phases. Furthermore, the crystalline phases are encircled by the amorphous phase, and there are almost no contact points between the two phases. The large crystalline areas consist of two different crystalline phases with differing chemical compositions. The lighter inner phase has to be formed first owing to its position. The surrounding darker phase could be an indication of peritectic solidification. Moreover, dendritic structures containing all components amid the amorphous phase are notable. Because of the position and appearance, it can be assumed that this structure solidified last from the supersaturated liquid phase, but is presumably not of importance for position welding and viscosity. The dark amorphous phase consists of SiO_2 , Al_2O_3 , Na_2O , MnO and F . Spectrum 5 is composed of chromium and titanium oxides, iron and nickel. Figure 5 summarises the described findings.

Fig. 11 Depiction of DTA curves for E308LT0-4 slag



On the basis of these observations, it is expected that the phases solidify in the numbering sequence. It is apparent that initially, the development of the crystalline phases prefers TiO_2 and ZrO_2 as the main components. Crystalline phase 1 exhibits the highest ZrO_2 contents with 44 m%. Thus, the amount of ZrO_2 in the liquid phase should decrease. This could explain the precipitation of the Cr_2O_3 - and MnO-rich crystalline phase 2.

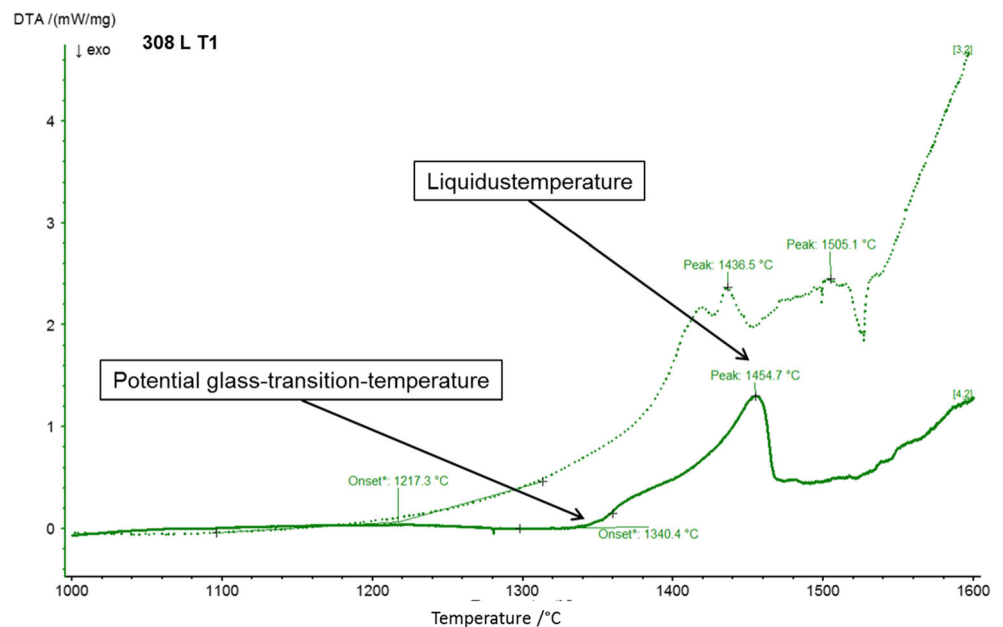
The comparatively high amounts of SiO_2 and MnO and the low content of TiO_2 in crystalline phase 3 are notable. Owing to the position and size of the phase, it is conceivable that parts

of the amorphous phase were energised by the EDX measurement.

3.5 E308LT1-4 type slag

Ti- and Cr-rich phases are found in the periphery zones of the crystalline areas and Zr is distributed throughout. The amorphous phase contains high contents of Si, Na, F and K. The distribution is shown in Fig. 6 and is similar to that for E308LT0-4.

Fig. 12 Depiction of DTA curves for E308LT1-4 slag



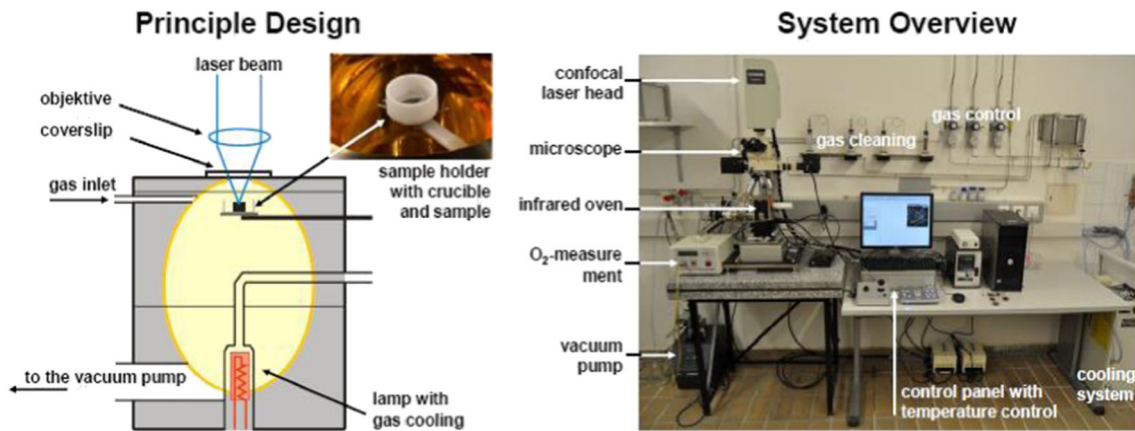


Fig. 13 HT-LSCM Yonekura VL 2000DX and Mirror furnace SVF 17 SP [24, 25]

Figure 7 shows the SEM images with different magnifications for various measurement points. The chemical compositions listed in Table 5 belong to the spectra shown in Fig. 7.

This slag also consists of three crystalline phases and one amorphous phase. In addition, metallic inclusions were detected (spectrum 2 in Fig. 7a and spectrum 3 in Fig. 7b). The dark appearing crystals composed of TiO_2 , ZrO_2 , Al_2O_3 and Cr_2O_3 (spectrum 3 in Fig. 7a and spectrum 6 in Fig. 7b) and are interlocked. Further, TiO_2 - and Cr_2O_3 -rich phases are discernible in the peripheral areas of the columnar crystals (spectra 4 and 5 in Fig. 7b). This configuration could indicate peritectic solidification. The light crystal phase appears in a fine dendritic structure with the main components Cr_2O_3 and TiO_2 , apart from MnO and ZrO_2 . Furthermore, another phase is detectable in spectrum 1 in Fig. 7a. From the appearance, position, and chemical analysis, this could be non-molten filler material. A simplified presentation of the mentioned descriptions is depicted in Fig. 8. The numeration of crystalline phases corresponds to the assumed sequence of formation.

The E308LT1-4 slag contains significantly higher TiO_2 contents in the crystalline phases compared to E308LT0-4 slag, which conforms to the chemical analyses via RFA. The

small amount of ZrO_2 indicates a tangential role of this component. The TiO_2 content decreases with the order of crystalline phase formation. The higher amount of TiO_2 in the T1 slag compared to the T0 slag is based on the higher rutile amount in the filling.

3.6 Determination of phase fractions in slags

By using the CEMEX software, the phase fractions were determined by the respective grey scale based on the higher magnification images. Figures 9 and 10 show the SEM images with a coloured depiction of the phases. The corresponding results are listed in Table 6.

The amorphous phase and the crystalline phase 2 exhibit the highest amounts of the phase fraction. Figure 10 shows the non-uniform distribution of the phases over the cross section and local differences in the distribution of phase 1.

3.7 Differential thermal analysis (DTA)

DTA was performed using a STA 449 F3 Jupiter and the evaluation was carried out using Proteus Analysis software.

Fig. 14 a Heat treatment procedure for reference measurement, b heat treatment at high temperatures

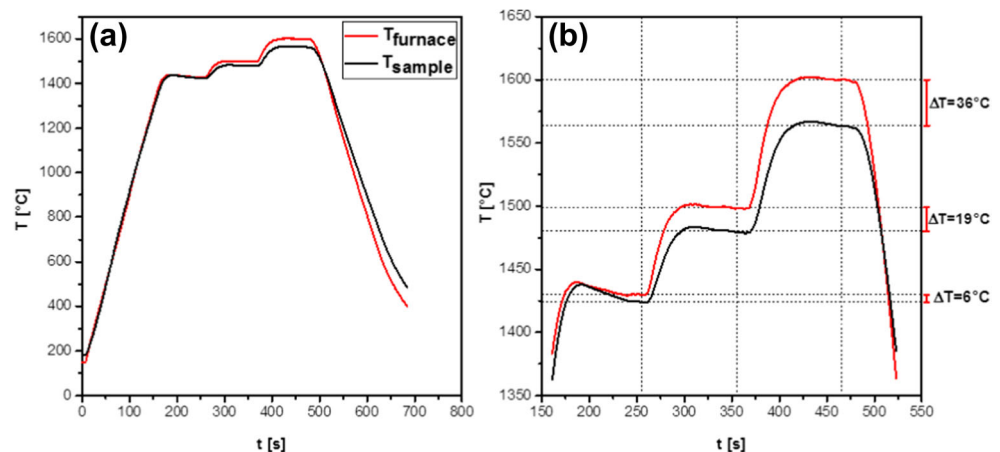
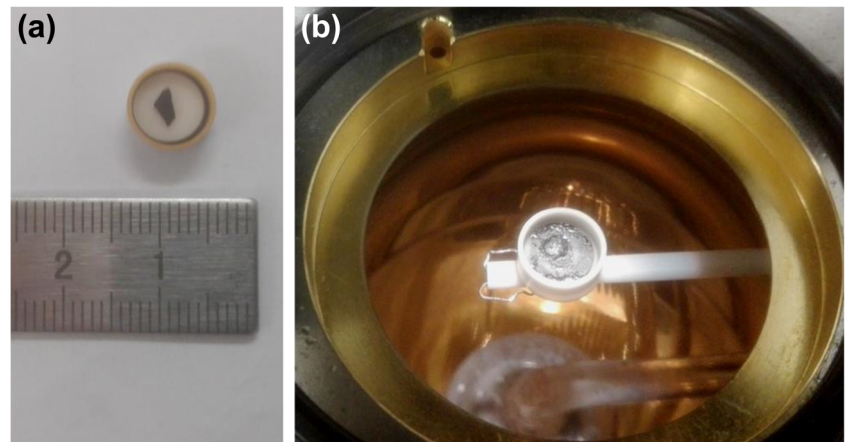


Fig. 15 Samples for HT-LSCM measurement **a** before and **b** after the investigations



The samples were exposed to an Ar environment in Pt/Ir crucibles. A heating rate of 5 K/min was employed, and a purge flow rate of 20 ml/min was applied. In preparation of measurements, the chamber was evacuated three times to avoid effects of the atmosphere. The samples were heated up to 1600 °C to guarantee a homogeneous, liquid slag. Measuring occurred during cooling from 1600 to 800 °C.

3.8 E308LT0-4 type slag

The DTA curves are shown in Fig. 11. A number of phase transformations occurred between 1260 and 1503 °C. It is not completely clear whether this is a solid-liquid transformation, a solid transformation or an evaporation of liquid components. The last peak occurred at 1502 °C, which represents the liquidus temperature. The first phase transformation starts at 1267 °C. From the SEM/EDX investigations, it can be assumed that this involves the glass-transition temperature of the amorphous phase. According to Angell and Sichina [23], the thermal capacity is decreased during the cooling of glasses when the glass transition temperature is exceeded. Thus, the

endotherm signals above 1267 °C signify a glass transition. Peaks occur between 1410 and 1460 °C. Owing to a partial overlap, it is conceivable that the peaks at 1441 and 1454 °C belong to one peak. Apart from investigations in argon atmosphere, measurements in nitrogen were performed, which is illustrated by the dotted line.

3.9 E308LT1-4 type slag

The E308LT1-4 sample shows a distinct solid-liquid transition. During this transition, three different crystalline phases precipitate with DTA-signals overlapping, which is assumed based on the OM and SEM investigations. The liquidus temperature is 1454 °C, and the onset of the phase transitions was determined to be at 1427 °C. A further onset was identified at 1340 °C, which could indicate the glass transition temperature. The curve is depicted in Fig. 12.

The E308LT0-4 and E308LT1-4 samples exhibit a further increase in the curve after the liquidus temperature is reached, which is characteristic for most slag systems owing to a reaction between the crucible and the slag.

Fig. 16 Start melting of amorphous phase at 520 ± 10 °C; and situation result at 1290 ± 10 °C

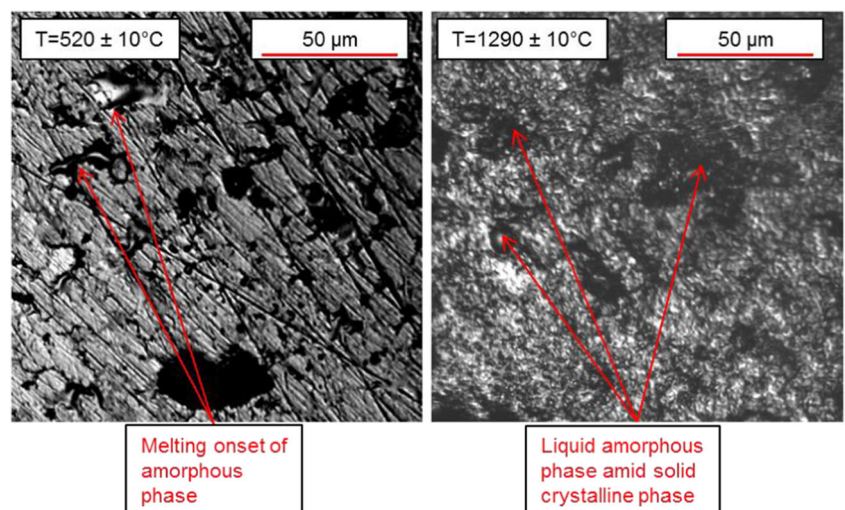
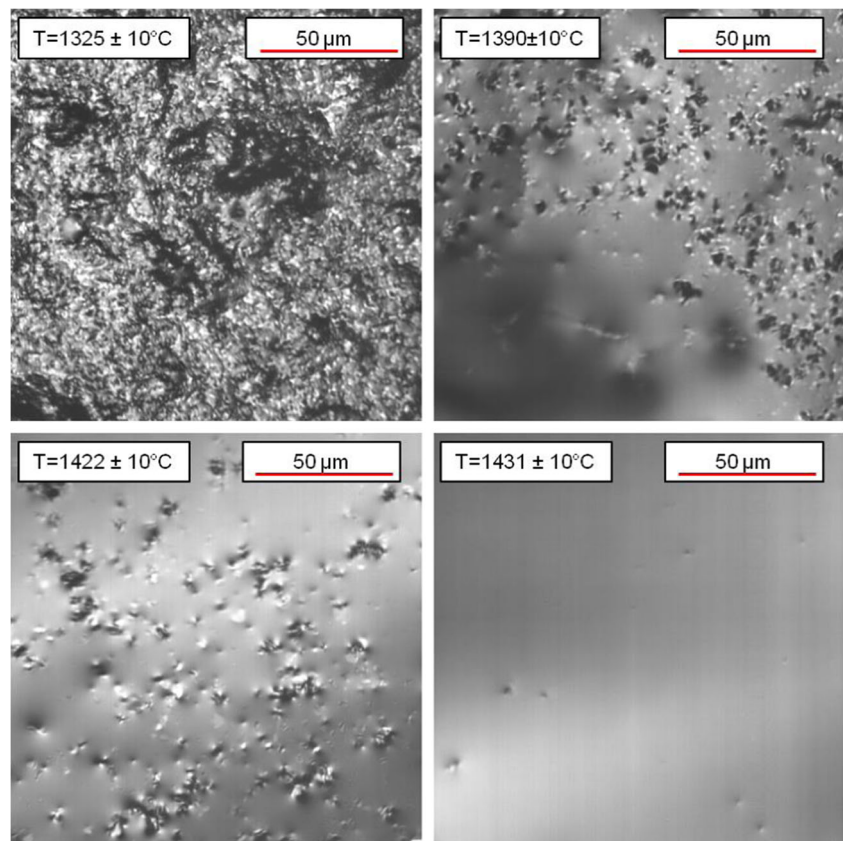


Fig. 17 Depiction of dissolution of crystalline phases



3.10 High-temperature laser scanning microscopy (HT-LSCM)

A Yonekura VL 2000 DX high-temperature laser scanning confocal microscope equipped with an SVF 17 SP mirror furnace (Fig. 13) was applied to directly observe the local interface migration on the surface of the sample (5 mm in diameter and 1 mm in height) during the cyclic phase transformation experiment.

To avoid oxidation on the surface of the sample, high-temperature laser scanning confocal microscopy (HT-LSCM) experiments were performed under a high-purity Ar 6.0 atm in Al_2O_3 crucibles. The experiments included heat treatment with extended hold times between 1430 and 1600 °C, as shown in Fig. 14. A reference temperature measurement was performed beforehand using a type S thermocouple, designated as T_{sample} .

At temperatures below 1450 °C, there were deviations of ± 10 °C between the actual and measured temperatures. Above 1400 °C, the measured values were higher than the actual ones. The difference increased with increasing temperatures.

The temperature intervals are sufficient to ensure melting of the samples. The appearance before and after the investigation is shown in Fig. 15.

All samples show discrepancy of the transition temperatures in the DTA values. It is conjectured that amorphous

phases do not possess a liquidus temperature but exhibit a glass transition temperature. Identification of the glass transition temperature is precluded; therefore, the amorphous phases can be identified as the liquid phase when the viscosity falls below a certain level.

3.11 E308LT0-4 type slag

The investigation reveals a clear distinction between the crystalline, amorphous and metallic phases. The crystalline phases cannot be differentiated more accurately due to their small phase sizes.

A liquid phase appears at a comparatively low temperature of 520 °C owing to the heating. This could not be determined via DTA. The other phase transitions exhibit a deviation of 50 °C compared to the DTA values. The size of the melting interval shows good conformity (cf. 90 and 106 °C). The following phases are observed:

- 25–1325 °C: Clearly visible liquefaction of amorphous phase fractions, surrounded by solid crystalline phases. Furthermore, a change in the appearance of the crystalline phases is detectable. This suggests possible minimal liquidation of the crystalline phases at temperatures below 1000 °C. Phase transitions in the

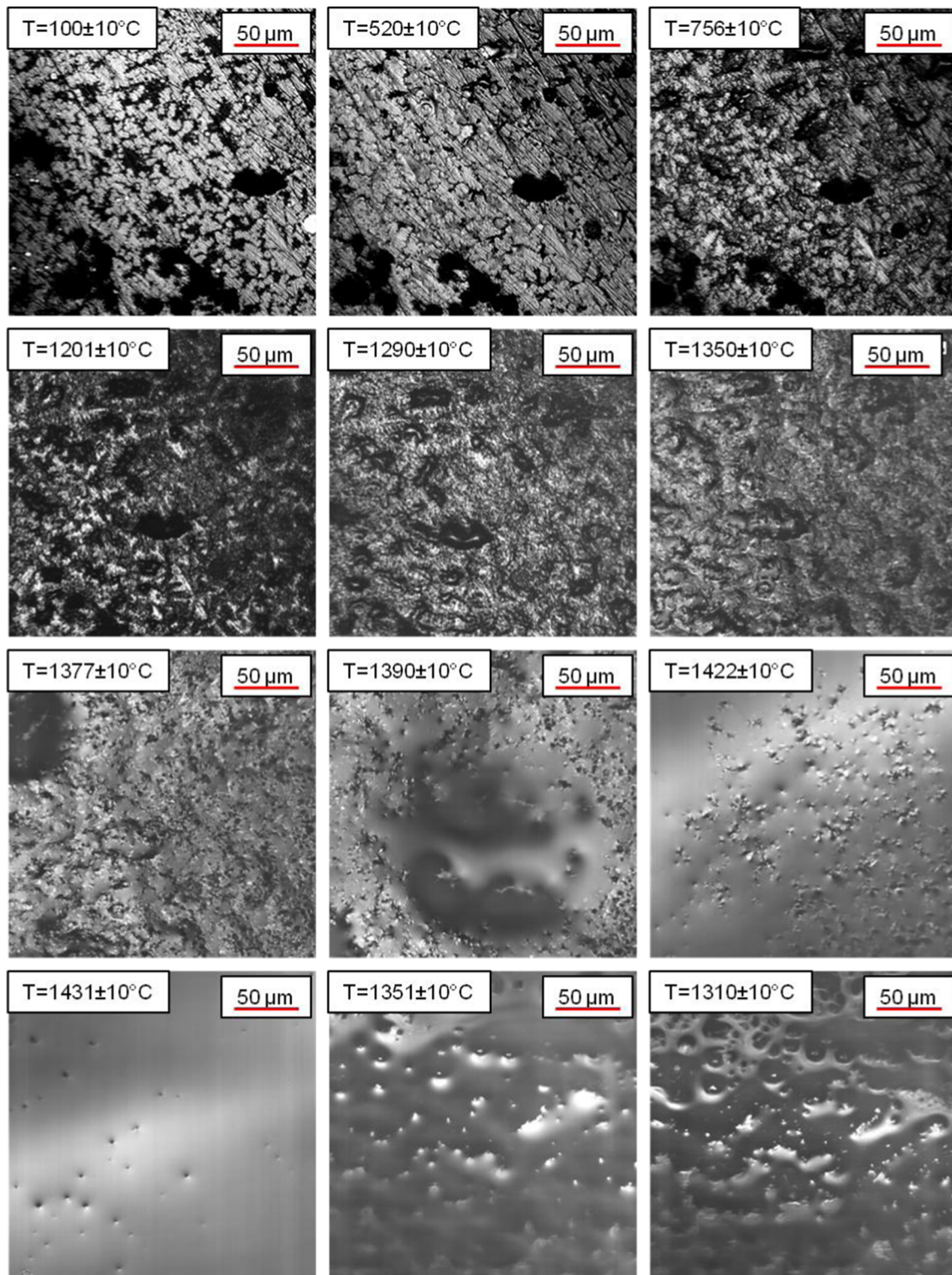


Fig. 18 HT-LSCM images

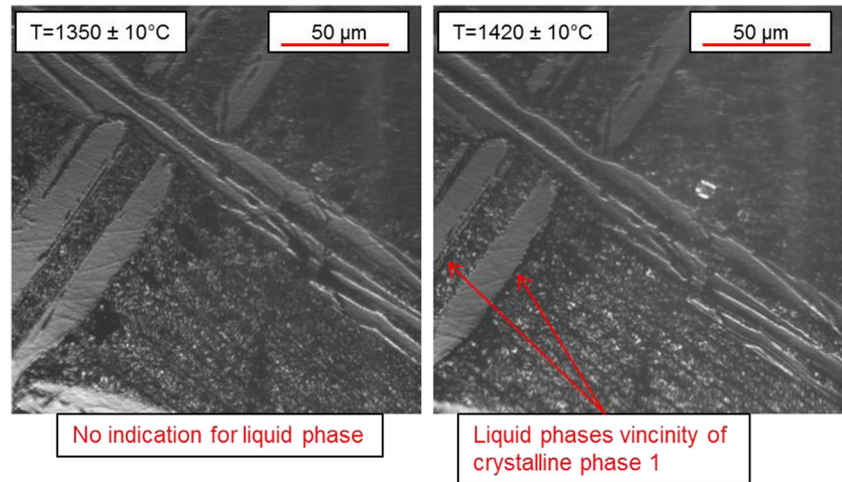
solid are conceivable. The associated images are shown in Fig. 16.

- 1325–1430 °C: Dissolution of the crystalline phases, clearly recognisable between 1422 and 1431 °C. The slag is completely liquefied at 1431 °C (Fig. 17).

3.12 E308LT1-4 type slag

Also in this case, the images of slag E308LT1-4 clearly distinguish between crystalline, metallic and amorphous phase fractions. Furthermore, crystalline phase 1 can be differentiated from

Fig. 19 E308LT1-4 slag appearance at 1350 ± 10 and 1420 ± 10 °C

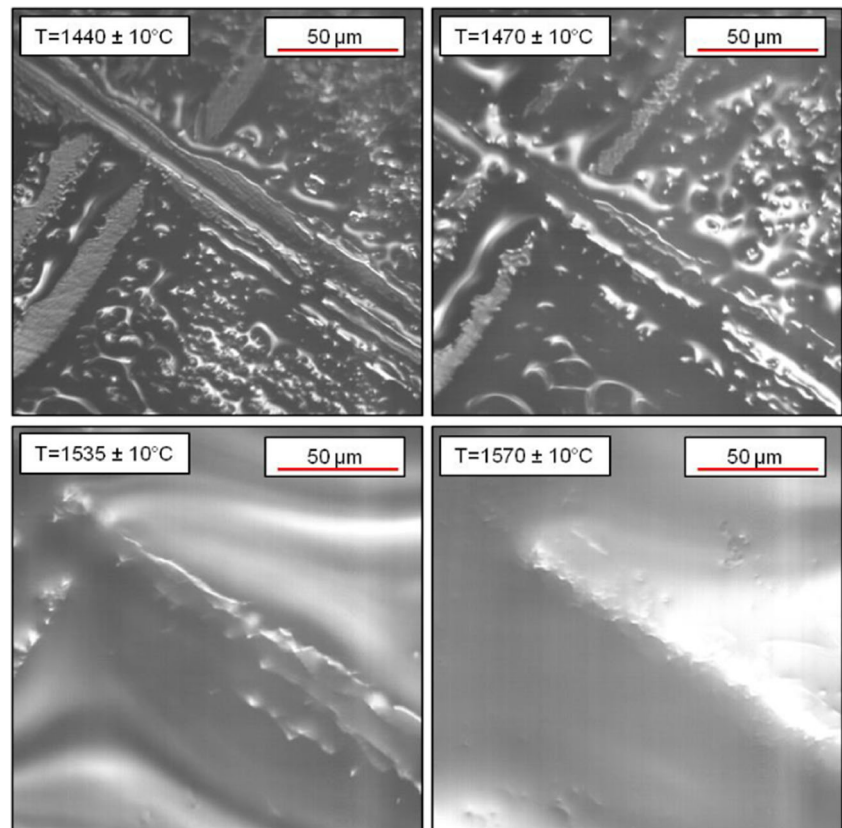


the remaining crystalline phases. A further distinction between crystalline phases 2 and 3 cannot be made (Fig. 18).

The transition temperatures are divergent to those determined via DTA. The differences are between 50 and 100 °C. Following phases were observed:

- 25–1420 °C: The appearance of solid phases change. Transformation of solid phases is conceivable.
- 1420–1440 °C: First liquid phases occur at 1420 °C, as shown in Fig. 19, but possible liquid phases at lower temperatures cannot be excluded.

Fig. 20 Depiction of dissolution of crystalline phases between 1440 and 1570 °C for E308LT1-4.



- 1440–1570 °C: When the temperature reaches 1440 °C, crystalline phases 2 and 3 dissolve until 1570 °C, as shown in Fig. 20.

3.13 Viscosity

The viscosities of the ‘liquid’ slag were determined using an Anton Paar Physica MCR 301 rotational viscometer (Fig. 21). The melting was carried out in Mo crucibles using Ar atmosphere at temperatures between 1550 and 1650 °C. After

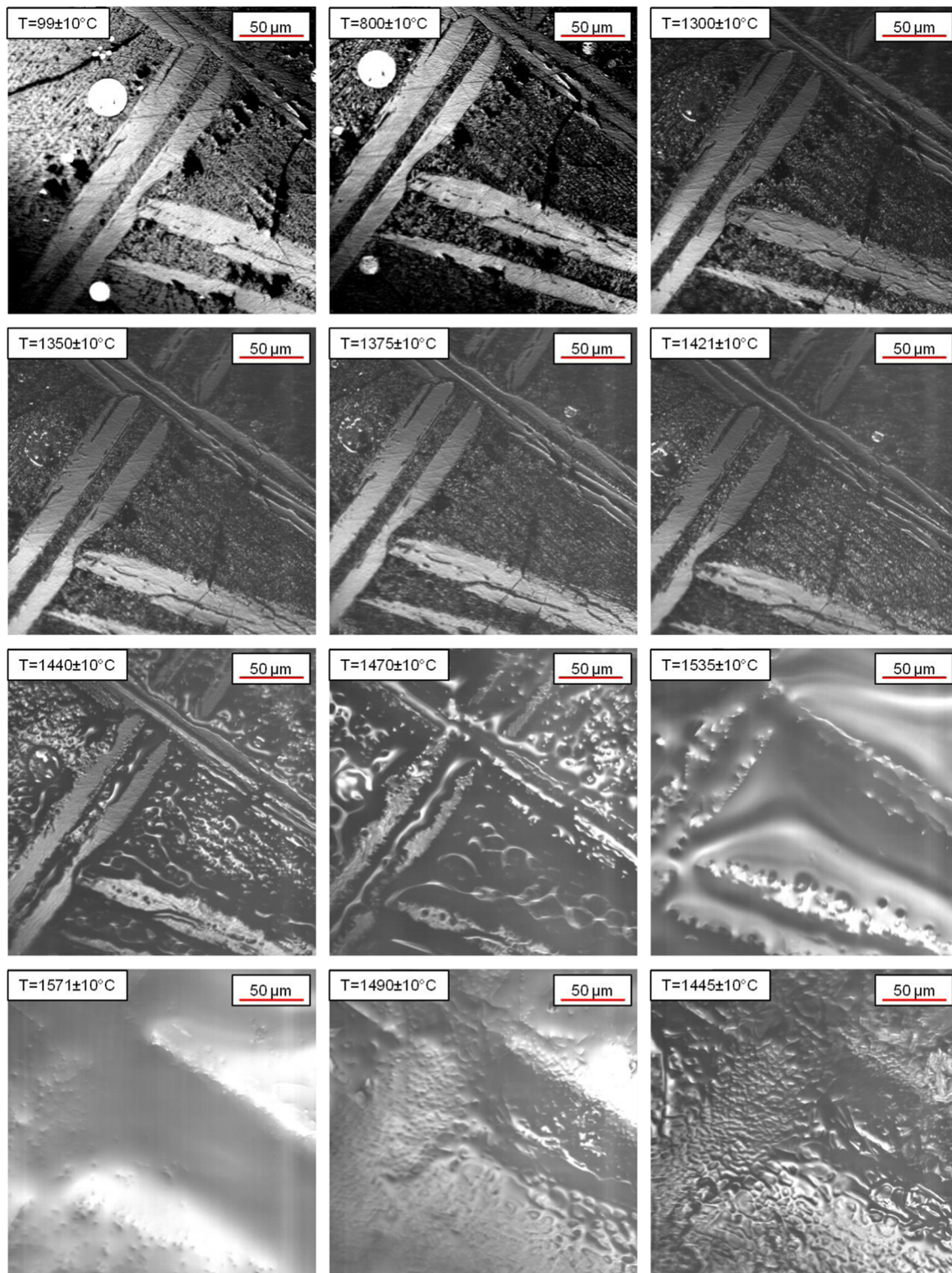


Fig. 21 HT-LSCM measurements for E308LT1-4.

applying the correct melt level, the samples were cooled in the furnace and supplied to the viscometer.

The heating and cooling of the samples were conducted in an induction furnace using the Linn High Therm frequency generator. The crucible was implanted in a

graphite element. The software RheoPlus was used for controlling and analysing the obtained data. Ar was passed by the bottom and top sides of the furnace at 200 and 60 l/min, respectively. The most important components are illustrated in Fig. 22.

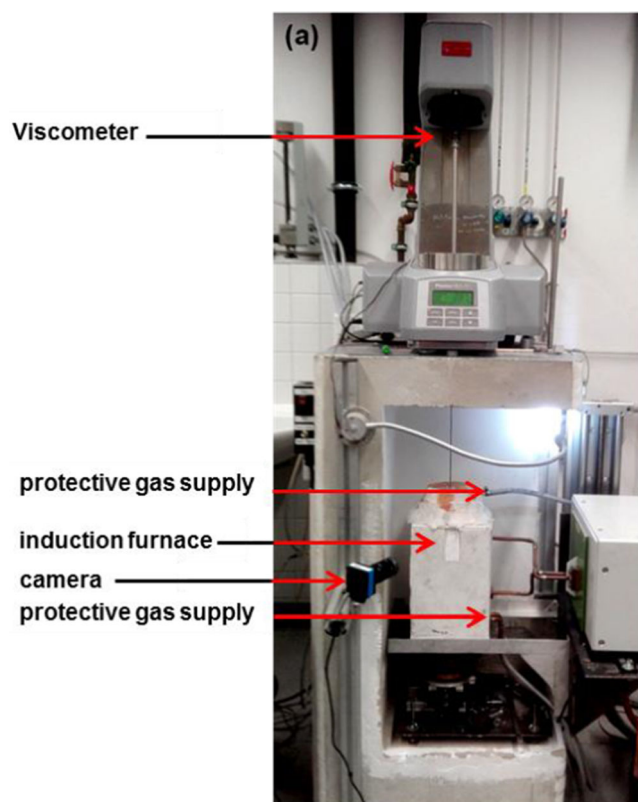
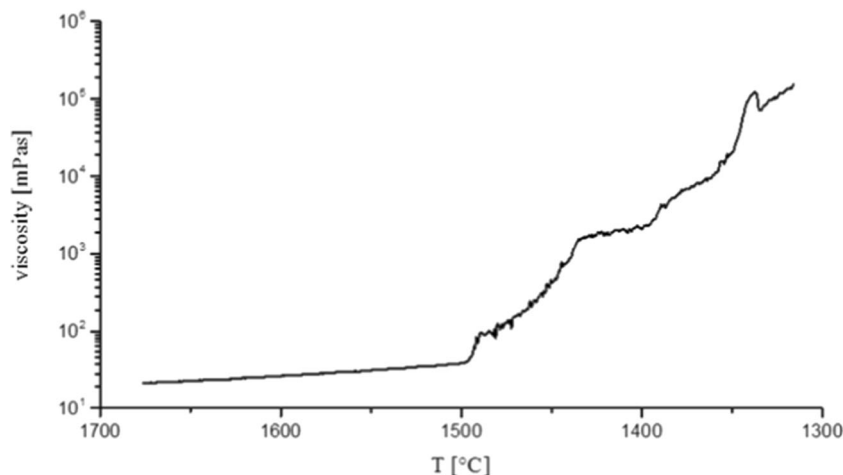


Fig. 22 Experimental setup with viscometer including furnace and agitator

The measurements were conducted with a cooling rate of 10 K/min. To ensure a constant temperature the sample was held for 10 min and then cooled continuously, while the viscosity was recorded. The rotation speed of the agitator was 30 U/min.

It has to be mentioned that the necessary remelting and cooling of the slag as part of the measurement cause a certain change in the slag composition compared to the origin slag resulting from the welding process, but as earlier investigations have shown, these influences are minor.

Fig. 23 Viscosity versus temperature based on a cooling rate of 10 K/min



Differences between the slags for the T0 position and T1 position welding are obvious in terms of the viscosity. The curve shapes versus temperature are different and shown in Figs. 23 and 24.

3.14 E308LT0-4 type slag

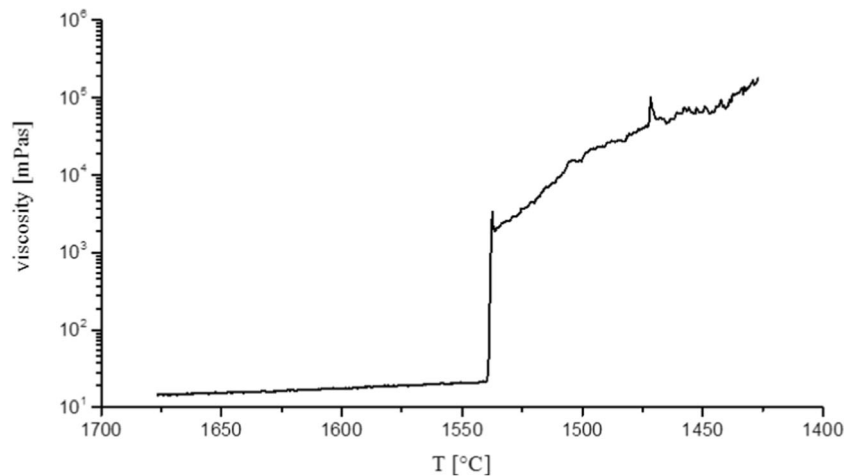
Figure 23 illustrates the measurement of the viscosity versus temperature based on a cooling rate of 10 K/min.

The curve of viscosity starts with a basic viscosity of 21 ± 0.5 mPas at 1675 °C. Subsequently, the viscosity suddenly increases from 40 to 75 mPas at 1495 °C, which indicates precipitation of the crystalline phase. The slag viscosity is largely constant between 1490 and 1483 °C. Further increases in the viscosity between 1480 and 1400 °C are detectable, which indicate the precipitation of more crystalline phases.

3.15 E308LT1-4 type slag

Figure 24 shows the viscosity measurement for E308LT1-4 versus temperature based on a cooling rate of 10 K/min. The viscosity starts with a basic viscosity of 14 ± 0.5 mPas at 1675 °C and reaches 21 ± 0.5 mPas until the break temperature at 1540 °C, where a sudden increase to 2100 mPas occurs within 3 °C (1540–1537 °C). Subsequently, the viscosity increases to the maximal measurable value of 200 Pas. The shape of the curve is typical for slags used for vertical welding and the sharp increase indicates the precipitation of the crystalline phases within a very narrow temperature interval. The fast solidification of the slag enables welding in vertical position. The further increase in viscosity after the break point can be attributed to the higher remaining melt viscosity and the slight decrease is caused by the replenishing melt.

Fig. 24 Viscosity versus temperature based on a cooling rate of 10 K/min



4 Discussion

The investigation showed that different phases exist within the different kinds of rutile slags. Apart from amorphous phases, various crystalline phases with varying compositions and metallic spatter were found. They mainly consist of TiO_2 , ZrO_2 , MnO and Cr_2O_3 . Comparisons with the constituents of binary and ternary systems indicate that the liquidus temperatures of the single constituents are higher than those of the slags. These findings suggest a dissolution of the phases in the course of heating, which explains the behaviour and appearance of the slags when compared to those in case of melting. This was also confirmed by HT-LSCM investigations. Thus, the solubility levels are exceeded during the cooling of the liquid slags. Therefore, certain crystalline phases precipitate from the slag. Hence, the slags have to be considered as an entire

system, within single phases that precipitate in certain stability ranges. The crystalline precipitates are noticeable by a viscosity increase due to the lower content of the remaining low-viscosity melt. This behaviour could also lead to a sudden viscosity increase during cooling.

The high contents of TiO_2 , ZrO_2 , etc., in the crystalline phases result in a reduction of these oxides in the remaining liquid melt. In contrast, the amount of the other components increase, which promotes a liquid phase at low temperatures.

The E308LT1–4-type slag has high contents of TiO_2 and Cr_2O_3 which induce higher crystalline contents in the solidifying slag. Therefore, lower amounts of SiO_2 , MnO , F , etc. occur as a result of the smaller proportion of the amorphous phases.

The occurrence of the various phases in the investigated 308L-type slags is schematically shown in Figs. 25 and 26,

Fig. 25 E308LT0-4 type slag: solid phase precipitation behaviour in relation to the viscosity change

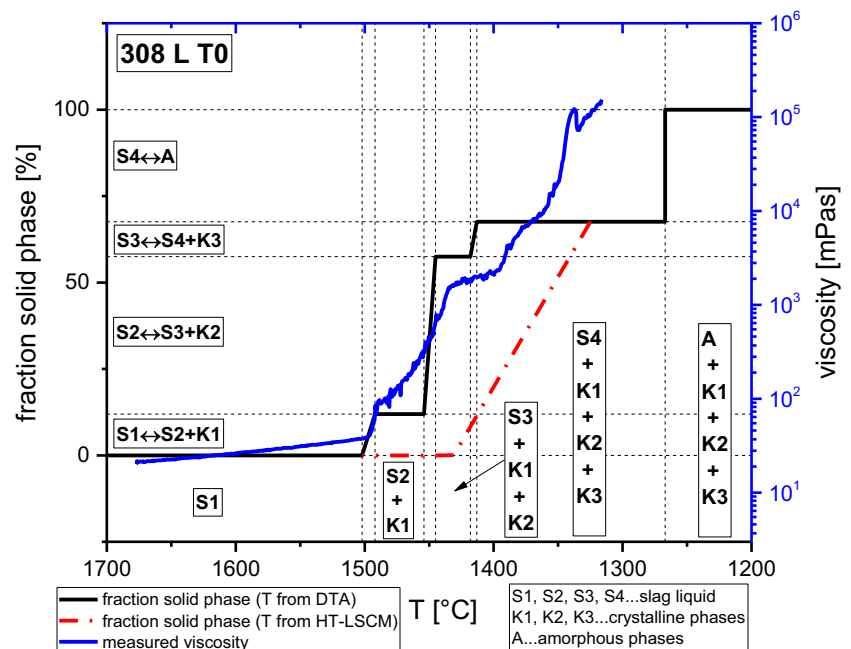
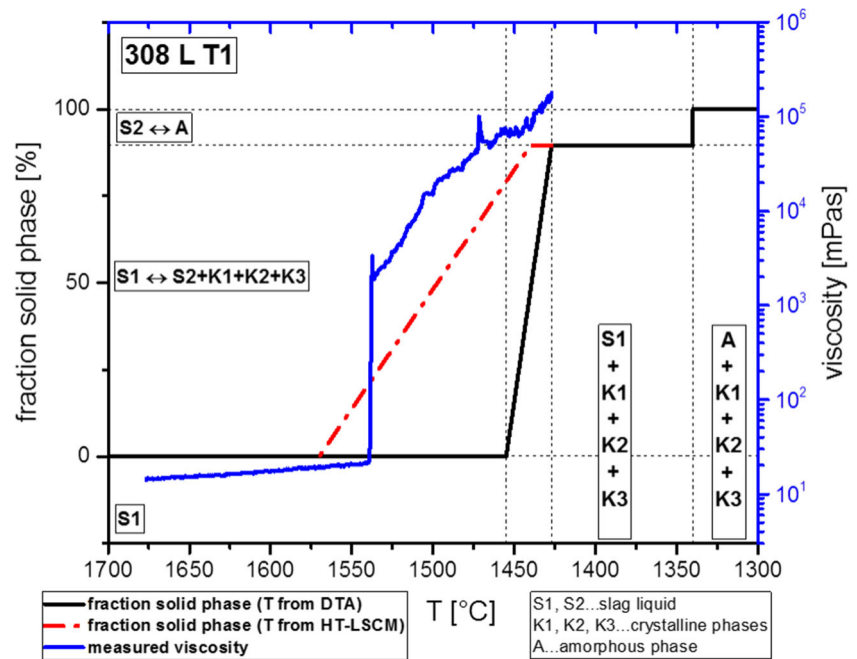


Fig. 26 E308LT1-4 type slag: solid phase precipitation behaviour in relation to the viscosity change



based on DTA measurements. The red dotted lines indicate HT-LSCM measurements. As it can be seen in the diagrams, the HT-LSCM measurement lines exhibit a lower slope. This is probably due to the use of entire slag pieces.

This comparison demonstrates that the knowledge of the existence of certain phases in solidifying slags, their fraction and precipitation temperature ranges enables a good estimation of the viscosity behaviour. The large crystalline phases grew together massively and require more time for dissolution compared to the powder used for DTA investigations. Furthermore, exact attribution of transition temperature to the dissolution of phase is complex. Thus, the temperatures measured from DTA are more plausible. Other deviations result from the cooling nature of viscosity measurements. Therefore, effects of nucleation and growth of certain phases are integrated.

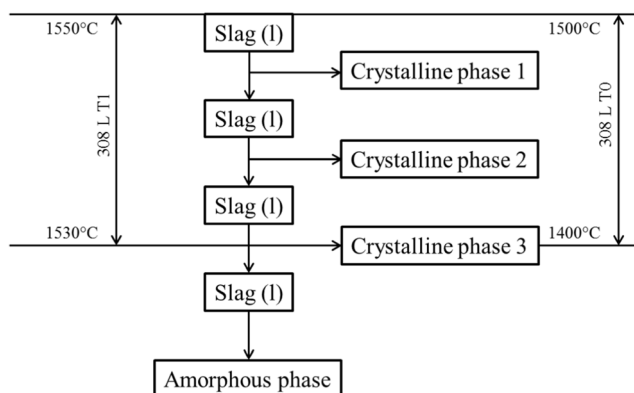


Fig. 27 Scheme of phases occurring in 308L-type welding slags

5 Summary

The slags of the two different high-alloyed flux-cored wires of type 308L differ in their chemical composition and their proportion of crystalline and amorphous phases. The E308LT1-4-type slag for vertical welding consists of 10–20% of amorphous phase, whereas E308LT0-4-type slag for horizontal welding has 32% of amorphous phase. Furthermore, all slags have the three crystalline phases, but with varied composition and different solidification temperature ranges. So E308LT1-4 type slag solidifies within a smaller temperature range. Combined with the higher amount of crystalline phases, this leads to a tremendous increase in viscosity. The amounts of certain crystalline phases of the E308LT1-4 type slag are small. Thus, it can be assumed that they do not play a crucial role in the viscosity of the slags. The investigation pointed out that the precipitation of a high amount of certain phases take place within a short temperature range in order to ensure position welding.

The DTA findings in respect to the precipitation temperatures of the different phases in the slags during cooling are summarised in Fig. 27. Moreover, the break and liquidus temperatures can be defined to be within a certain range ($T_{\text{Break}} \approx T_{\text{Liquidus}} + 50^\circ\text{C}$).

It has to be mentioned that these two examples of flux-cored wires for stainless steel electrodes are not representative for all such state-of-the-art flux cored electrodes. They differ for instance in containing components like titanium and zirconium dioxide. Thus, they may exhibit other welding characteristics.

Funding information The authors gratefully acknowledge financial support from the K1-MET GmbH Metallurgical Competence Centre. The research program of the K1-MET Competence Centre is supported by COMET (Competence Centre for Excellent Technologies), the Austrian program for competence centres. COMET is funded by the Federal Ministry for Transport, Innovation, and Technology, the Federal Ministry for Science, Research and Economy, the provinces of Upper Austria, Tyrol, and Styria as well as the Styrian Business Promotion Agency (SFG).

References

1. Strassburg F W, Wehner H, Schweißen nichtrostender Stähle, 4., überarb. u. erw. Aufl., DVS-Vlg, Düsseldorf, 2008
2. Mills KC, Yuan L, Jones RT (2011) Estimating the physical properties of slags. *J South Afr Inst Min Metall* 111(10):649–658
3. Verein Deutscher Eisenhüttenleute (VDEh) (1995) Slag atlas, 2nd edn. Verlag Stahleisen, Düsseldorf
4. Mysen BO (1988) Structure and properties of silicate melts. Elsevier, Amsterdam
5. Santhy K, Sowmya A, Sankaranarayanan SR (2005) Effect of oxygen to silicon ratio on the viscosity of metallurgical slags. *ISIJ Int* 45(7):1014–1018
6. ISO 11357-2 (2013) Plastics – differential scanning calorimetry – part 2: determination of glass transition temperature. <https://www.iso.org/standard/57966.html>
7. Verein Deutscher Eisenhüttenleute (VDEh), Ausschuss für Metallurgische Grundlagen (1981) Slag atlas. Verlag Stahleisen, Düsseldorf
8. Flood H, Förland T (1947) The acidic and basic properties of oxides. *Acta Chem Scand* 1:592–604
9. Kekkonen M, Oghbasilasie H, Louhenkilpi S (2012) Viscosity models for molten slags, research report, Aalto University. Helsinki, Finland <https://aaltodoc.aalto.fi/bitstream/handle/123456789/3640/isbn9789526046037.pdf?sequence=1&isAllowed=y>
10. Urbain G, Cambier F, Deletter M, Anseau MR (1981) Viscosity of silicate melts. *Trans J Br Ceram Soc* 80(4):139
11. Bauné E, Bonnet C, Liu S (2000) Reconsidering the basicity of a FCAW consumable-part 1: solidified slag composition of a FCAW consumable as a basicity indicator. *Weld J* 79(3):57s–65s
12. Mills K (2011) The estimation of slag properties: short course presented as part of Southern African Pyrometallurgy, <http://www.pyrometallurgy.co.za/KenMills/index.html>, Abgerufen am: 04.08.2016
13. Schwemmer DD, Olson DL, Williamson DL (1979) The relationship of weld penetration to the welding flux. *Weld J* 58(5):153s–160s
14. Herasymenko P (1938) Electrochemical theory of slag-metal equilibria. Part I.—reactions of manganese and silicon in acid open-heart furnace. *Trans Faraday Soc* 34(0):1245–1254
15. Sohn I, Wang W, Matsuura H, Tsukihashi F, Min DJ (2012) Influence of TiO₂ on the viscous behavior of calcium silicate melts containing 17 mass% Al₂O₃ and 10 mass% MgO. *ISIJ Int* 52(1):158–160
16. Mysen B, Neuville D (1995) Effect of temperature and TiO₂ content on the structure of Na₂Si₂O₅-Na₂Ti₂O₅ melts and glasses. *Geochim Cosmochim Acta* 59(2):325–342
17. Mills K, Guo M (2014) The importance of materials properties in high-temperature processes. *ISIJ Int* 54(9):2000–2007
18. Kondratiev A, Jak E, Hayes PC (2002) Predicting slag viscosities in metallurgical systems. *JOM* 54(11):41–45
19. Mills KC (1993) The influence of structure on the physico-chemical properties of slags. *ISIJ Int* 33(1):148–155
20. Iida T, Sakai H, Kita Y, Shigeno K (2000) An equation for accurate prediction of the viscosities of blast furnace type slags from chemical composition. *ISIJ Int* 40(Suppl):S110–S114
21. Mills KC, Sridhar S (2013) Viscosities of ironmaking and steelmaking slags. *Ironmak Steelmak* 26(4):262–268
22. Zhang S, Zhang X, Peng H, Wen L, Qiu G, Hu M, Bai C (2014) Structure analysis of CaO–SiO₂–Al₂O₃–TiO₂ slag by molecular dynamics simulation and FT-IR spectroscopy. *ISIJ Int* 54(4):734–742
23. Angell CA, Sichina W (1976) Thermodynamics of the glass transition: empirical aspects. *Ann N Y Acad Sci* 279(1 The Glass Tra):53–67
24. Presoly P, Pierer R, Bernhard C (2012) Linking up of HT-LSCM and DSC measurements to characterize phase diagrams of steels. *IOP Conf Ser: Mater Sci Eng* 33:1–9
25. Urbain G (1987) Viscosity estimation of slags. *Steel Res* 58(3):111–116